IEEE Access
Multidisciplinary ⋮ Rapid Review ⋮ Open Access Journal

Received 8 December 2022, accepted 20 December 2022, date of publication 22 December 2022,
date of current version 29 December 2022.

Digital Object Identifier 10.1109/ACCESS.2022.3231812

RESEARCH ARTICLE

Scalable Modeling of Human Blockage at Millimeter-Wave: A Comparative Analysis of Knife-Edge Diffraction, the Uniform Theory of Diffraction, and Physical Optics Against 60 GHz Channel Measurements

SWAGATO MUKHERJEE[1], GREGORY SKIDMORE[1], TARUN CHAWLA[1], (Member, IEEE), ANMOL BHARDWAJ[2,3], CAMILLO GENTILE[2], (Member, IEEE), AND JELENA SENIC[2,4]

[1]Remcom, State College, PA 16801, USA
[2]Radio Access and Propagation Metrology Group, NIST, Gaithersburg, MD 20899, USA
[3]Department of Chemistry and Biochemistry, University of Maryland, College Park, MD 20742, USA
[4]Department of Physics, University of Colorado, Boulder, CO 80309, USA

Corresponding author: Swagato Mukherjee (swagato.mukherjee@remcom.com)

ABSTRACT Human blockage at millimeter-wave frequencies is most commonly modeled through Knife-Edge Diffraction (KED) from the edges of the body shaped as a vertical strip. Although extensively validated in controlled laboratory experiments, the model does not scale to realistic 3D scenarios with many, randomly oriented bodies, on which multipath signals can be incident from any direction, not just normal to the strip. To address this, in this article we investigate computational electromagnetic methods based on raytracing. In addition to the KED method, we compare the Uniform Theory of Diffraction (UTD) and Physical Optics (PO) methods against an extensive suite of precision channel measurements at 60 GHz. And in addition to the vertical strip, cylinder and hexagon body shapes are considered with the UTD method, and a 3D phantom shape is considered with the PO method. We found that the PO method is the most accurate, but also the most computationally intensive due to the large number of faces (approximately 8000) in the phantom and due to the inherent complexity of the method itself. While the UTD method with the hexagon shape (approximately 42 faces) is slightly less accurate than the PO method, it provides the best compromise when efficiency is paramount.

INDEX TERMS Raytracing, KED, UTD, PO, human shadowing, mmWave, *WaveFarer*.

I. INTRODUCTION

The insatiable demand for wireless spectrum has prompted rapid development of fifth-generation (5G) technology that exploits the swaths of bandwidth available in the millimeter-wave (mmWave) regime to deliver Gigabits/second data rates [1], [2]. The 60 GHz band – precisely 57 GHz to 71 GHz – is particularly appealing, as much due to its ultrawide bandwidth as to its unlicensed usage. One disadvantage of mmWave signals is susceptibility to blockage by smaller objects like humans, cars, and foliage by virtue of the shorter wavelength [3], [4], [5]. Pervasive blockage from humans is a primary concern, especially when designing wireless systems slated for deployment indoors and in urban open streets [6], [7]. A critical part of that design is an accurate channel propagation model. Several analytical models have been proposed to predict human blockage in terms of body shape, size, and material [8], [9], [10], [11], [12], [13], [14], [15], [16], [17], [18], [19], [20], [21]. Alternatively, there are strictly empirical models in the literature that provide

The associate editor coordinating the review of this manuscript and approving it for publication was Gerardo Di Martino.

best-fit statistical distributions to measurements [20], [22], [23]. Neither category, however, is generalizable enough to any scene geometry. Barring a few works [12], [24], [25], most develop simple 2D analytical or empirical models to predict blockage from a single human that is placed in the same vertical plane as the transmitter (Tx) and the receiver (Rx). Though some analytical models can be extended to 3D scenarios, their rigid architecture is incompatible with the complex geometry associated with multiple, randomly oriented humans and other small objects in the environment, and with several Tx and Rx units.

Numerical electromagnetic solvers based on the ray-tracing method are accurate, extendable to 3D scenarios, and computationally efficient. They also support the non-stationarity of objects (pedestrian and vehicular motion, etc.) in the scene. What is more, they furnish complementary information such as angle-of-arrival, angle-of-departure, angle-of-incidence, complex impulse response, polarization characteristics, etc. From this information, a statistical description of typical human blockage parameters used for developing communication protocols – decay time and rise time, average fade duration, fade depth – can be calculated. Although raytracing is more computationally expensive than simple analytical or empirical models, graphics processing unit (GPU)-based ray-tracing available today makes it ever the choice by network designers thanks to its ability to accurately model complex real-life scenarios and the host of information it provides. In this article, we investigate ray-tracing solutions available in Remcom's *WaveFarer*®[1] radar simulation tool [26] to predict human blockage and compare the predictions against 60 GHz measurements collected by the National Institute of Standards and Technology (NIST) [27]. The major contributions of this article are threefold. We compare predictions against measurements for the following:

1) Knife-Edge Diffraction (KED) methods: Analysis shows that the incremental complexity of the multiple KED method [14], [16], [28] is justified over the simpler double KED method [10] only when the additional edge(s) fall within the first Fresnel zone radius.
2) The Uniform Theory of Diffraction (UTD) method: Two different shapes for the human body are considered, namely a cylinder and a hexagon, and the hexagon is shown to perform the best. The hexagon shape is further refined to obtain better agreement with the measurements.
3) Physical Optics (PO) method: A 3D phantom shape for the human body is considered with the PO method to provide an upper bound on performance when compared to the KED and UTD methods.

[1]Certain commercial equipment, instruments, or materials are identified in this paper in order to specify the experimental procedure adequately. Such identification is not intended to imply recommendation or endorsement by the National Institute of Standards and Technology, nor is it intended to imply that the materials or equipment identified are necessarily the best available for the purpose.

The remainder of the article is organized as follows: Section II describes the measurement campaign performed by NIST. Section III presents the human body shapes found in the literature that are pertinent to this work. Section IV details the KED, UTD, and PO prediction methods, and Section V presents the results obtained when comparing the three methods to the measurements. Finally, Section VI concludes the article.

II. CHANNEL MEASUREMENTS

The channel sounder used to collect measurements is described in detail in [29]; here we provide a brief overview. An arbitrary waveform generator at Tx synthesizes a pseudo-random noise (PN) code with 2047 chips, each chip 0.5 ns in duration, equivalent to 2 GHz bandwidth. The code is modulated through binary phase-shift keying (BPSK) at an intermediate frequency (IF), upconverted to precisely 60.5 GHz, and then transmitted through a vertically polarized horn antenna with a 22.5° Gaussian beam pattern and 18.1 dBi gain. At the Rx end, the signal is received by the same antenna type,[2] downconverted back to IF, digitized at 40 Gigasamples/s, and then correlated with the known PN code to generate a complex channel impulse response. The complex amplitude of the first peak in the response is used as the Rx signal for analysis, comprising both the LoS (line-of-sight) ray (when unobstructed) and any diffracted rays from the body. The ceiling and ground bounces fell out of the beamwidth of the antennas and any other multipath from the surrounding environment arrived later in the response. An optical cable provided phase synchronization between the Tx and Rx.

A single measurement scenario consisted of a human subject walking 1.5 m from *Start* to *Stop*, as depicted in Fig. 1(a), along a linear trajectory perpendicular to the LoS path between the Tx and Rx. The antenna heights were both fixed at 1.6 m. A photograph of the channel sounder during data collection is shown in Fig. 1(c). Per scenario, the Rx signal was sampled 1500 times over the 5 s period that the human walked along the linear trajectory, corresponding to 5 samples per wavelength, generating the characteristic signal profile shown for an example scenario in Fig. 2. Here the Rx signal is converted to shadow loss, defined as the signal power relative to the far end of the completely flat power profile (normalized to 0 dB). Shadow loss has three regions: the pre-shadow, the shadow, and the post-shadow. The shadow region is where the LoS ray is obstructed by the human body and is defined in the signal profile between the peak before the Rx signal drops precipitously to the peak after it rises back from the drop. The region before (after) the shadow region is termed the pre- (post-) shadow region. As in other works, motion parallel to the LoS path was not considered as it effects little to no variation in the signal profile for characterizing different regions. Other parameters in Fig. 2 are

[2]Although the Tx and Rx feature an array of horn antennas, only one at each end was activated for these measurements: the ones pointed towards each other.

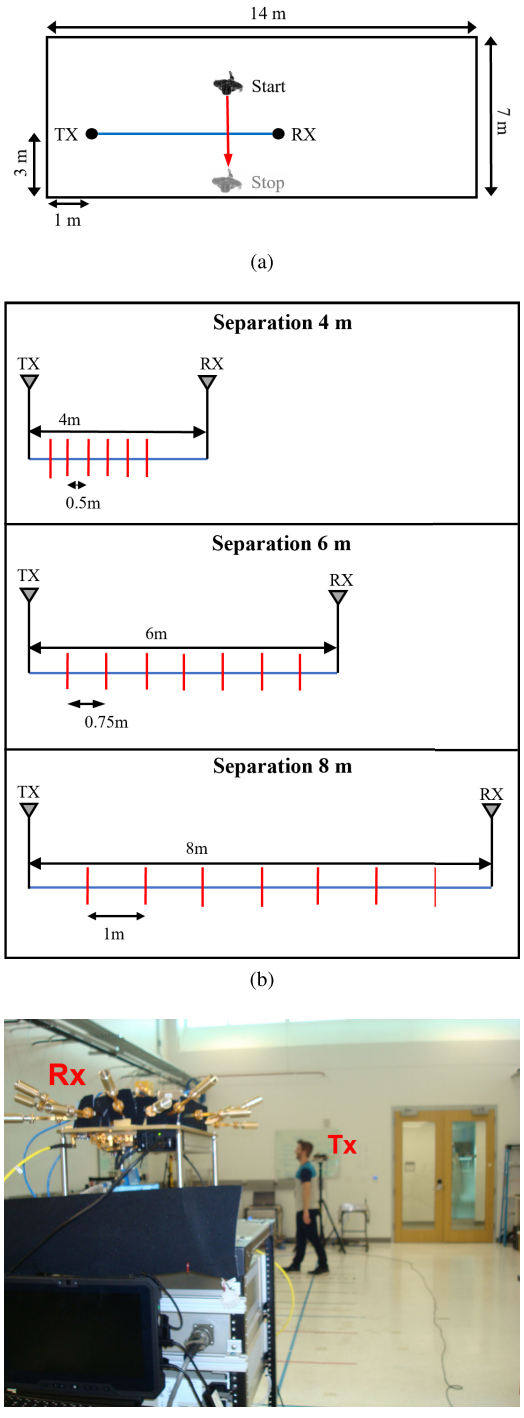

FIGURE 1. Measurement campaign. (a) Diagram of measurement set-up with human traversing a linear trajectory perpendicular to the LoS ray between the Tx and Rx [27]. (b) Assortment of walking trajectories marked with red ticks for each of the three Tx-Rx separations. (c) Photograph snapped during a measurement with one of the three human subjects [27].

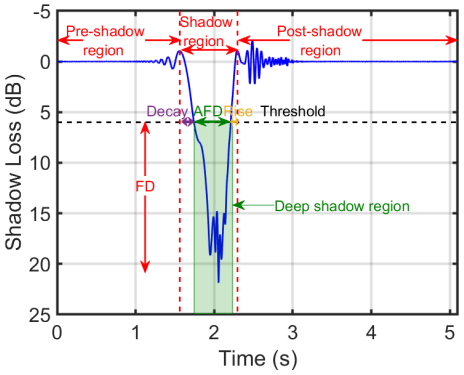

FIGURE 2. Typical parameters used to characterize human shadowing, overlaid on a sample measured signal profile (blue).

TABLE 1. Body dimensions of human subjects.

Human Subject	Height, H_t (m)	Body Depth, B_d (m)	Body Width, B_w (m)	Head Depth, H_d (m)	Head Width, H_w (m)
A	1.83	0.26	0.50	0.25	0.17
B	1.72	0.25	0.47	0.24	0.16
C	1.68	0.23	0.42	0.22	0.16

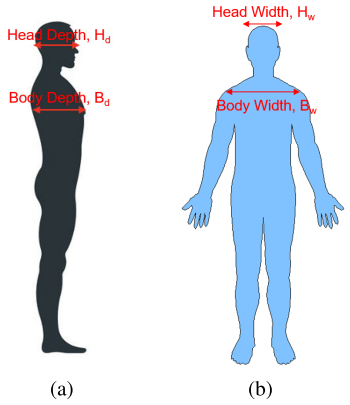

FIGURE 3. (a) Sideview and (b) Frontview of the human body with the body dimensions as defined in Table 1.

introduced in Sec. V-D. The walking speed of each human subject was about 0.3 m/s, regulated by a metronome. The measurement scenarios had the following parameters:

1) Three human subjects with different body structure and heights. The heights, the body (head) depths and widths are tabulated in Table 1 and shown in Fig. 3.
2) Tx-Rx distances of 4m, 6m, and 8m.
3) Measurement tracks at incremental crossing distances between the Tx and Rx, with six increments for the 4 m distance, and seven for the 6 m and 8 m distances (see Fig. 1(b)).

These combinations resulted in a total of 60 measurement scenarios.

III. HUMAN BODY SHAPES

A shape commonly found in literature to model the human body is the infinitely long vertical strip, depicted in Fig. 4(a). Diffraction occurs when an incident ray – from the LoS path

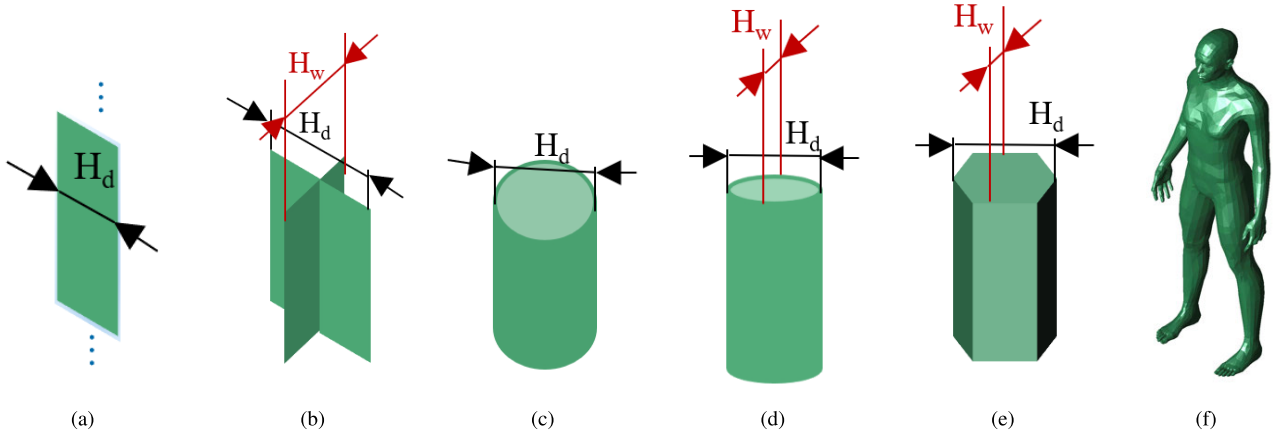

FIGURE 4. Human body shapes: (a) vertical strip, (b) double vertical strip (c) cylinder (d) elliptic cylinder (e) hexagon (f) phantom.

or from any other multipath in the environment – is normal to the face. The width of the strip is set to the depth of the human subject under inspection. Since the vertical strip captures only one dimension of the human body, a more accurate shape for off-normal incidence is the double vertical strip, which features two orthogonal strips of different widths that intersect at the center, as depicted in Fig. 4(b). The double vertical strip is not infinitely long; rather it has an additional edge on top to model diffraction from the head and/or another edge on the bottom to model diffraction from the feet. Note that these two shapes are accurate only when the incident ray is normal to the face(s), and hence they fail in realistic 3D scenarios due to the abundance of multipath incident from any direction.

To extend application of the vertical strip to realistic 3D scenarios, human bodies have been modeled as cylinders and elliptic cylinders [28], [30], [31], shown in Fig. 4(c) and Fig. 4(d) respectively. The elliptic cylinder is a generalized cylinder that can be scaled in two dimensions to capture the orientation of the body with respect to the incident ray. The hexagon in Fig. 4(e) is included in this work as an alternative to the cylinder shapes and, as the elliptic cylinder, can also be scaled in two dimensions. As we shall see later, the hexagon outperforms the cylinder and is thus recommended for modeling the human body. Since the cylinder and hexagon shapes have more faces than the vertical strip, naturally they are more computational intensive.

The last shape that we consider is the 3D phantom, shown in Fig. 4(f). The number of faces can range between hundreds to thousands depending on the amount of detail preferred, therefore it is the most computationally intensive shape.

IV. PREDICTION METHODS

The three prediction methods we consider are described in the following subsections, along with their advantages and disadvantages.

A. KNIFE-EDGE DIFFRACTION

Knife-edge diffraction on the human body modeled as a vertical strip is by far the most popular method to predict human blockage. The special case in which blockage is modeled as knife-edge diffraction from the two edges of the infinitely long vertical strip is referred to in the literature as the double KED (DKED) method [10]. Rather, when blockage is modeled as knife-edge diffraction from the top, bottom, and sides of the the double vertical strip, it is referred to as the multiple KED (MKED) method [14], [16], [28].

The knife-edge method assumes that the vertical strip is completely absorbing and in the DKED [10] the received field is estimated as the sum of the diffracted fields from the edges of the strip. The diffraction coefficient for any given edge is calculated using the Fresnel-Huygens principle [32] expressed through the following equations

$$k_{edge} = \frac{1+j}{2}\left\{\left(\frac{1}{2}-C(v_{edge})\right)-j\left(\frac{1}{2}-S(v_{edge})\right)\right\} \quad (1)$$

$$v_{edge} = \pm h_{edge}\sqrt{\frac{2}{\lambda}\left(\frac{1}{d_A}+\frac{1}{d_B}\right)}, \quad (2)$$

where $C(v_{edge})$ and $S(v_{edge})$ are the cosine and sine Fresnel integrals, h_{edge} is the distance from the Tx-Rx line to the edge, d_A and d_B are the distances from the Tx to the strip and from the strip to the Rx respectively, as shown in Fig. 5, and λ is the signal wavelength. The $\pm$ sign associated with v_{edge} is applied with a $+$ sign to both edges in the shadow region, and in the pre- and post- shadow regions the edge farthest from the incident ray is assigned a $+$ sign while the one closest is assigned a $-$ sign. Then the complex received field is given by

$$E_{Rx} = \frac{\lambda}{4\pi(d_A+d_B)} e^{\frac{-j2\pi}{\lambda}(d_A+d_B)} \sum_{edge=1}^{n_{edge}} k_{edge} \quad (3)$$

For DKED, $n_{edge} = 2$ in (3). A phase-corrected expression for the received field is often used in literature [27] instead

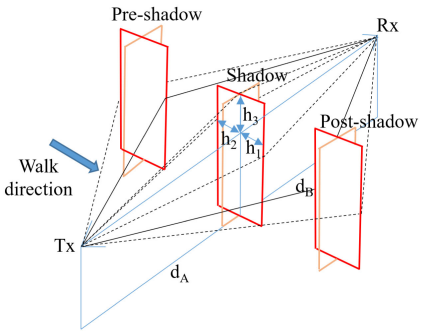

FIGURE 5. Graphical representation of the MKED method shown in the pre-shadow, shadow, and the post-shadow regions (the black dashed lines represent rays in the shadow region, while the black solid lines represent rays outside the shadow region).

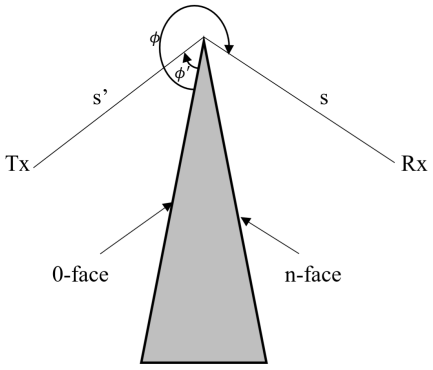

FIGURE 6. Diffraction from a wedge located between a Tx and Rx.

of (3). However in our work here, we found both versions to result in similar received fields, so no phase correction was applied.

Instead of considering a single vertical strip for modeling the human body as in the DKED model, the MKED method in [14] and [16] utilizes the double vertical strip of Fig. 4(b). The wider of the two strips as seen by the incident ray is chosen for calculating diffraction from the sides. As with the DKED, the received field is given by the sum of the diffracted fields from the edges; however, unlike the DKED, the MKED in [14] and [16] includes the top edge of the strip to model the head and/or the bottom edge [28] to model the feet, in addition to the two side edges. Thus, in the MKED method $n_{edge} = 3$ or $n_{edge} = 4$ in (3).

The benefit of the KED methods is their low computational expense and ease of implementation. However, as they are typically applied to vertical strips, their real-world applicability is limited and, to our knowledge, they have never been used to predict shadowing from more than three persons [24], [25]. Finally, KED methods do not consider material properties of the shadowing objects nor polarization of the incident rays.

B. UNIFORM THEORY OF DIFFRACTION

In contrast to the KED methods, the Uniform Theory of Diffraction does consider material properties and polarization of the incident rays. In the UTD method, the diffracted field [32] from the tip of a wedge, as shown in Fig. 6, is calculated as

$$E_{Rx} = E_0 \frac{e^{-jks'}}{s'} D^{\perp/\parallel} \sqrt{\frac{s'}{s(s+s')}} e^{-jks}, \tag{4}$$

where $D^{\perp}$ and $D^{\parallel}$ are the diffraction coefficients for the perpendicular and parallel polarizations respectively, E_0 is the free-space electric field, $k = \frac{2\pi}{\lambda}$ is the free-space wavenumber, s' is the distance from the Tx to the tip of the wedge, and s is the distance from the tip of the wedge to the Rx. The diffraction coefficient [27] is further given by

$$\begin{aligned} D^{\perp/\parallel} = \frac{-e^{\frac{j\pi}{4}}}{2n\sqrt{2\pi k}} \times \Bigg\{ & \cot\left(\frac{\pi + (\phi - \phi')}{2n}\right) \\ & \cdot F\left(kLa^{+}(\phi - \phi')\right) + \cot\left(\frac{\pi - (\phi - \phi')}{2n}\right) \\ & \cdot F\left(kLa^{-}(\phi - \phi')\right) + R_0^{\perp/\parallel} \cot\left(\frac{\pi - (\phi + \phi')}{2n}\right) \\ & \cdot F\left(kLa^{-}(\phi + \phi')\right) + R_n^{\perp/\parallel} \cot\left(\frac{\pi + (\phi + \phi')}{2n}\right) \\ & \cdot F\left(kLa^{+}(\phi + \phi')\right) \Bigg\} \end{aligned} \tag{5}$$

The function $F(.)$ is the Fresnel integral given as

$$F(x) = 2j\sqrt{x}e^{jx} \int_s qrt(x)^{\infty} e^{-jt^2} dt \tag{6}$$

and the other quantities in (5) are given as

$$L = \frac{ss'}{s+s'} \tag{7}$$

$$a^{\pm}(\beta) = 2\cos^2\left(\frac{2n\pi N^{\pm} - \beta}{2}\right) \tag{8}$$

$$\beta = \phi \pm \phi' \tag{9}$$

where $n\pi$ defines the exterior wedge angle and $N^{\pm}$ are integers that satisfy the following equations:

$$2\pi n N^{+} - \beta = \pi, \quad 2\pi n N^{-} - \beta = -\pi. \tag{10}$$

Finally, $R_0^{\perp/\parallel}$ and $R_n^{\perp/\parallel}$ in (5) are the Fresnel reflection coefficients for the perpendicular and parallel polarizations on the 0- and n-face of the wedge respectively.

The UTD enables modeling diffraction from a scattering object with arbitrary shape but well-defined edges – *e.g.* the hexagon-shaped human body – via the wedge-diffracted fields. Note that in the shadow region the total electric field is given only by the diffracted field, whereas in the illuminated region the diffracted field is added to the geometric optics (GO) fields to compute the total field. Analogous closed-form expressions can also be derived for diffraction from cylinders [28], [30] and elliptic cylinders [31]; however,

(4) and (5), which are widely used in existing literature [8], [9], [15], [28], and the expressions for diffraction from cylinders [28], [30], [31], are applicable for normal incidence only and as such can only describe scattering for 2D geometry.

To describe scattering for 3D geometry, the UTD method for oblique incidence [32] can be applied; due to complexity, the equations are omitted here. Implementation of the equations on arbitrary 3D shapes is even more complex, favoring numerical methods like raytracing. Remcom's *WaveFarer* ray-tracing suite can model 3D shapes and include multipath and shadowing generated by incident rays from any direction. In *WaveFarer*, rays interact with a scattering object's face in three ways: when the ray impinges on the face of an object, it can either reflect or transmit, and when it impinges on the edge of an object's face, the ray diffracts. The allowed interaction types and the number of interactions per ray determine the computation time. Reflection interactions propagate rays further, while transmissions can split them into an additional ray that refracts through a material. Diffractions, on the other hand, consist of cones of rays that emanate from an edge, generating thousands of new rays upon each diffraction, significantly increasing both the time incurred to perform raytracing as well as the time to process the increased number of rays. Hence for analyzing larger scenes with UTD, object shapes that capture the shadowing effects accurately through one diffraction per ray are preferred. This makes the hexagon and cylinder shapes ideal candidates for the UTD method.

C. PHYSICAL OPTICS

One limitation of the UTD method is degradation in accuracy when predicting diffraction from curved surfaces, particularly if the shape has more than one radius of curvature, as is true for spherical surfaces such as the head and shoulders. The PO method models scattering from such surfaces more precisely than the UTD method, by performing a surface integration that incorporates the sizes and shapes of the small faces that form these surfaces. In the PO method, the scattered field is computed from the surface currents on the scattering object induced by the incident GO fields. The scattered far-fields are obtained from these surface currents by performing radiation integrals. The scattered field computation can be mathematically expressed through the vector potentials [32] given as

$$\mathbf{A} = \frac{\mu}{4\pi}\iint_S \mathbf{J}_S \frac{e^{-jkR}}{R} dS' \tag{11}$$

$$\mathbf{F} = \frac{\epsilon}{4\pi}\iint_S \mathbf{M}_S \frac{e^{-jkR}}{R} dS' \tag{12}$$

where $\mathbf{A}$ and $\mathbf{F}$ are the far-field vector potentials, $\mathbf{J}_s$ is the surface electric current density, $\mathbf{M}_s$ is the surface magnetic current density, ϵ is the electric permittivity, μ is the magnetic permeability, and R is the radial distance between the source and the observation point. In turn, the scattered far-field electric ($\mathbf{E}_{scat}$) and magnetic ($\mathbf{H}_{scat}$) fields are given by

$$\mathbf{E}_{scat} \approx -j\omega\mathbf{A} - \frac{1}{\epsilon}\nabla \times \mathbf{F} \tag{13}$$

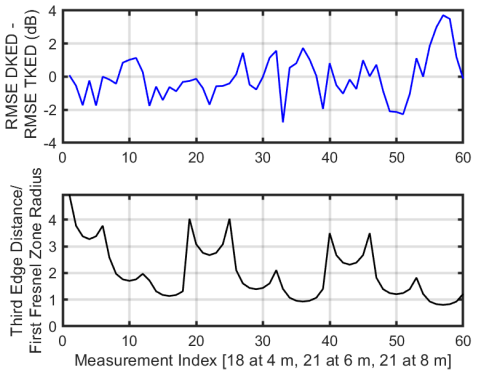

FIGURE 7. Difference in the RMSE between the TKED and DKED methods when compared to measurement (solid blue line) and the plot of ratio of the third edge distance to the first Fresnel zone radius (solid black line) for each measurement.

$$\mathbf{H}_{scat} \approx -j\omega\mathbf{F} + \frac{1}{\mu}\nabla \times \mathbf{A} \tag{14}$$

where ω is the angular frequency. Since the GO surface currents are approximate in nature and do not capture non-uniformity of the current densities close to an edge, a technique such as the method of equivalent currents [26] must be used to add the effect of these current densities to the PO scattered field solution. Note that the PO method only computes the scattered field at the Rx; to compute the total field, the incident field at the Rx without the scattering object must be added.

Since the PO method requires a surface integral to compute the scattered far-fields and another line integral to correct for the fields at the edges, it generally takes longer than the UTD method: in testing with *WaveFarer*, the PO method took up to two times longer simulation time than the UTD method (utilizing one diffraction per ray) when both methods were applied to the simple hexagon and cylinder, yet they returned comparable results; when the PO method was applied to the complex, finely-faceted phantom, it took up to five times longer. Hence only when accuracy is paramount and complex shapes are available is the PO method recommended, as its run time is significant. Recall that comparison to a single measurement scenario requires 1500 simulations (one per sample), so the PO method is not scalable to a larger scene that includes many structures and people. However it does provide an upper bound on performance accuracy.

V. RESULTS

First, we compare the MKED method to the DKED method and specify when the greater complexity of the former is warranted. Secondly, we compare the traditional DKED method to a hybrid DKED method recently proposed, showing that the latter is unnecessary for modeling shadowing from a human body. Next, we compare the shadowing predicted by the UTD method between the hexagon and cylinder shapes. In the last subsection, we compare results obtained by the three methods.

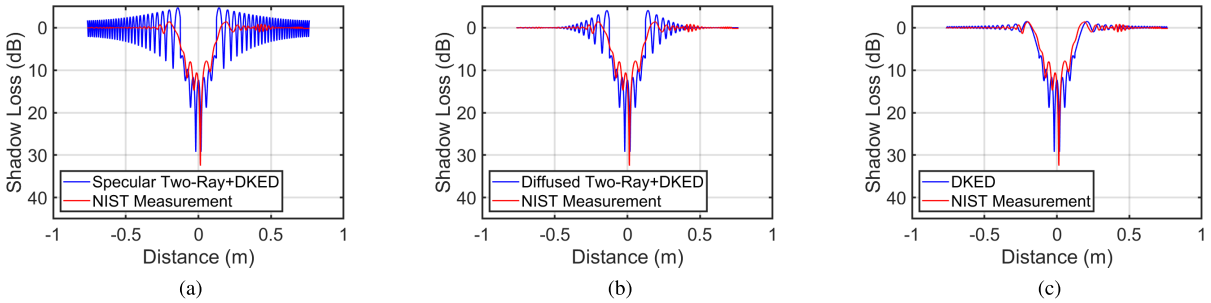

FIGURE 8. Comparison of shadow loss simulated with a (a) specular two-ray reflection method and (b) diffused two-ray reflection method used in the pre- and post-shadow regions and the DKED method used in the shadow region (solid blue line) to NIST measurement (solid red line). (c) Comparison of the DKED method prediction (solid blue line) to measured values (solid red line).

A. COMPARISON BETWEEN THE MKED AND THE DKED METHODS

Both the MKED and DKED methods have been cited numerous times in the literature [11], [15], [17], [28], yet it is still unclear when one or the other should be applied. To investigate this, we implemented the MKED method with three edges, as shown in Fig. 5, and refer to it as the TKED. Based on the walking direction and the location of the Tx-Rx setup in Fig. 5, the two side edges of the red strip generated diffraction in the shadow region. The top of the red strip was included as the third edge to capture the effect of diffraction from the head; accordingly, ν_{edge} in (2), corresponding to the top, always fell in the shadow region and so is assigned a $+$ sign. Since the feet are in contact with the floor, there is no well-defined edge at the bottom from which diffraction can take place. Therefore, the bottom edge was discarded.

We simulated shadow loss for all 60 measurement scenarios using the DKED and the TKED. Note that the Gaussian beam patterns of the Tx and Rx antennas were incorporated in the predictions for maximum fidelity. Next, we computed the root mean square error (RMSE) of the DKED and the TKED when compared to measurements and plotted their difference indexed per scenario in the upper subplot of Fig. 7; in the lower subplot, we plotted the ratio of the third-edge distance to the first Fresnel zone radius. The third-edge distance is simply the difference between the height of the human subject (see Table 1) and the height of the Tx and Rx (1.6 m). The first Fresnel zone radius is given by $F_1 = \frac{\lambda d_A d_B}{d_A + d_B}$. From Fig. 7, a significant difference in the RMSEs between the two methods (more than 2 dB) is observed only when the third edge is within or close to the first Fresnel zone radius. Thus, we can infer that unless the third (or any other) edge lies within F_1, no difference will be observed between the MKED and DKED. Interestingly enough, [27] also found two peaks in the Doppler spectrum generated from the same measurements studied here. This suggests that for these measurements, the DKED is sufficiently accurate. Yet, we still recommend the MKED when the third and or/fourth edge is close to or within the first Fresnel zone.

B. COMPARISON BETWEEN THE DKED AND A HYBRID DKED METHOD

A hybrid method was proposed in [27], in which shadow loss is predicted by a modified DKED method in the shadow region and by a two-ray reflection method in the pre- and the post-shadow regions. The reflection coefficient in the pre-shadow and the post-shadow regions is derived from the Fresnel equations [33], assuming the vertical strip shape. The two-ray method is shown to predict shadow loss accurately in the pre- and post-shadow regions [27] with empirically derived relative permittivity values of the body. However, when we implemented the same method for human skin relative permittivity $\epsilon_r = 8 - 9.5j$ reported in [34] for 60 GHz, we obtained the plot in Fig. 8(a), which disagreed with the measurements in these regions. Instead of specular reflection coefficients, we also tried the reduced reflection coefficient obtained by multiplying the Miller-Brown reflection reduction factor [35] (assuming an RMS height of 5 mm for the skin roughness) with the Fresnel coefficients to get the diffused two-ray prediction of shadow loss in Fig. 8(b). Even so, we still found disagreement, especially at the boundaries of the shadow region, as shown in Fig. 8(b). We therefore found no benefit of the hybrid method over the DKED or TKED methods for predicting blockage, especially since the latter two already achieve excellent agreement with the measurement in all three regions, as shown in Fig. 8(c).

C. COMPARISON BETWEEN THE CYLINDER AND HEXAGON SHAPES WITH THE UTD METHOD

The cylinder shape for the human body in Fig. 4(c) is the most popular for application with the UTD method [8], [9], [28], yet here we demonstrate that the hexagon shape in Fig. 4(e) actually yields better performance. The dimensions of the cylinder and hexagon were matched in diameter to the head dimensions in Table 1, as well as in height. The results from the predictions on both shapes are compared to the measurements in Fig. 9(a). Though both shapes overestimate the fade depth, the hexagon (RMSE = 6.82 dB) significantly outperforms the cylinder (RMSE = 9.44 dB). To capture diffraction from the head, a top edge was included in both

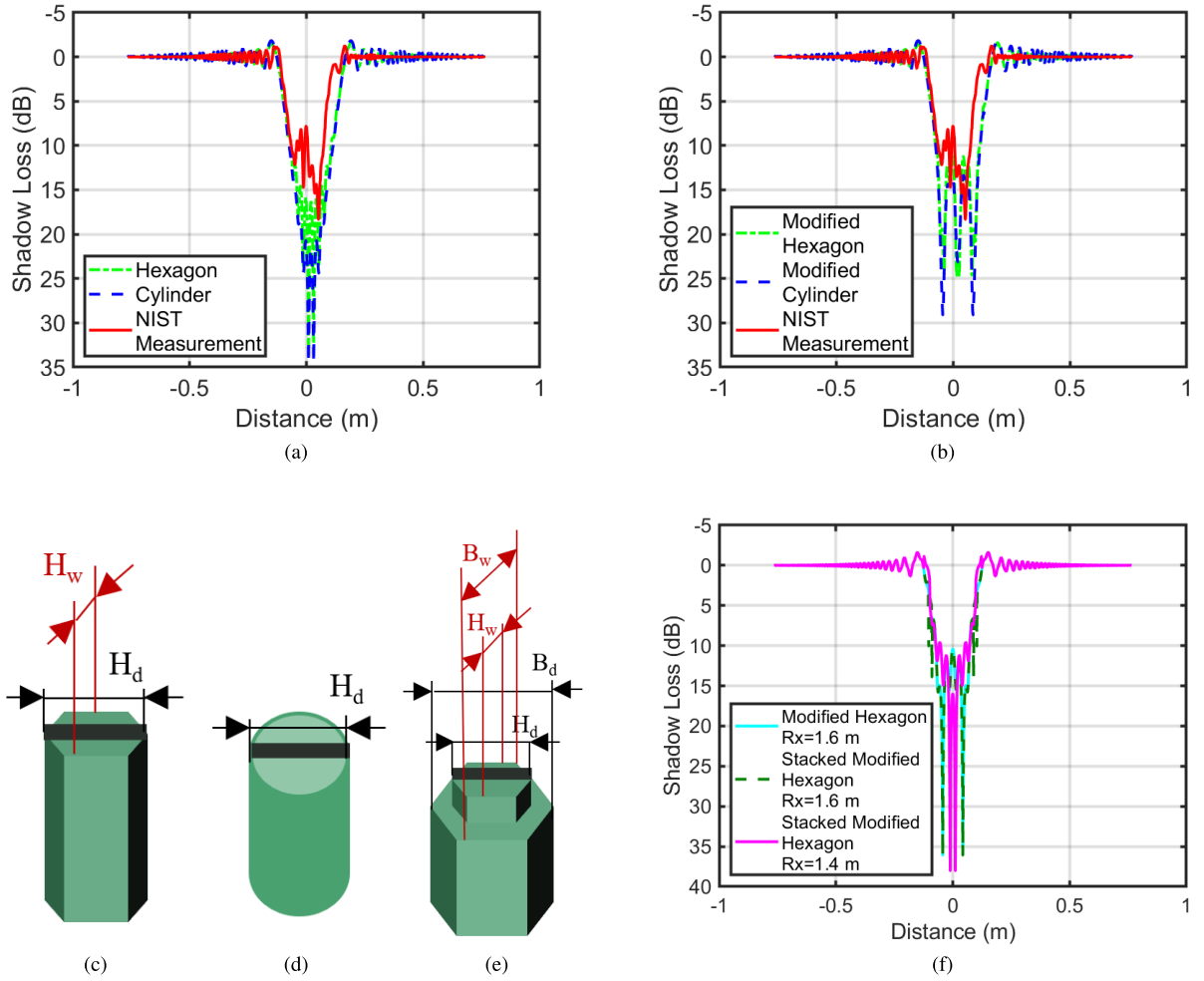

FIGURE 9. Comparison of shadow loss predicted with a (a) hexagon (green dash-dotted line) and cylinder (dashed blue line), (b) modified hexagon (green dashed line) and modified cylinder (blue dashed line) simulated using UTD and raytracing in *WaveFarer* to NIST measurement (solid red line). (c) Modified hexagon, (d) Modified cylinder, (e) Stacked modified hexagon and (f) Shadow loss computed for modified hexagon (cyan line) and stacked modified hexagon (green dashed line) for Rx height of 1.6 m and that computed for stacked modified hexagon (magenta line) for Rx height of 1.4 m.

shapes, as depicted in Fig. 9(c) and Fig. 9(d), while still running the UTD predictions with one diffraction per ray. The total height of the shapes with the top edge was again matched to the heights in Table 1. Shadow loss obtained with the modified hexagon and cylinder is plotted in Fig. 9(b). Indeed, we found that inclusion of the top edge reduces over-estimation by about 5 dB in both, yet the modified hexagon (RMSE = 6.85 dB) still outperforms the modified cylinder (RMSE = 7.97 dB). We also found that shadowing was dominated by the head due to Tx and Rx in the measurements at about the same height as the head; that is why the shapes were scaled to the head depths. However, for general Tx and Rx heights, the stacked hexagon depicted in Fig. 9(e) is recommended, as it better mimics the human body. Since the Tx and Rx heights are close to the head of the human subjects here, shadow loss predicted by the stacked modified hexagon model (Fig. 9(e)) is same as that predicted by the single modified hexagon model (Fig. 9(c)). This is shown to be true in Fig. 9(f). Hence, all results corresponding to the UTD method reported here were obtained by using the single modified hexagon model. However, if the Rx height was lower (for example, Rx height=1.4 m), the stacked modified hexagon model would predict a different shadow loss. Thus, future measurements at lower Rx heights can help to confirm the stacked model as a more general shape to model human body.

D. COMPARISON BETWEEN THE THREE PREDICTION METHODS

Next, we compare how well the three methods predict four typical parameters used to characterize shadow loss – decay time, rise time, average fade duration (AFD), and fade depth (FD) – against the measurements. The decay (rise) time is defined as the time interval from the highest peak just before (after) the shadow region to when the received signal first falls below (last rises above) a chosen threshold; the AFD is

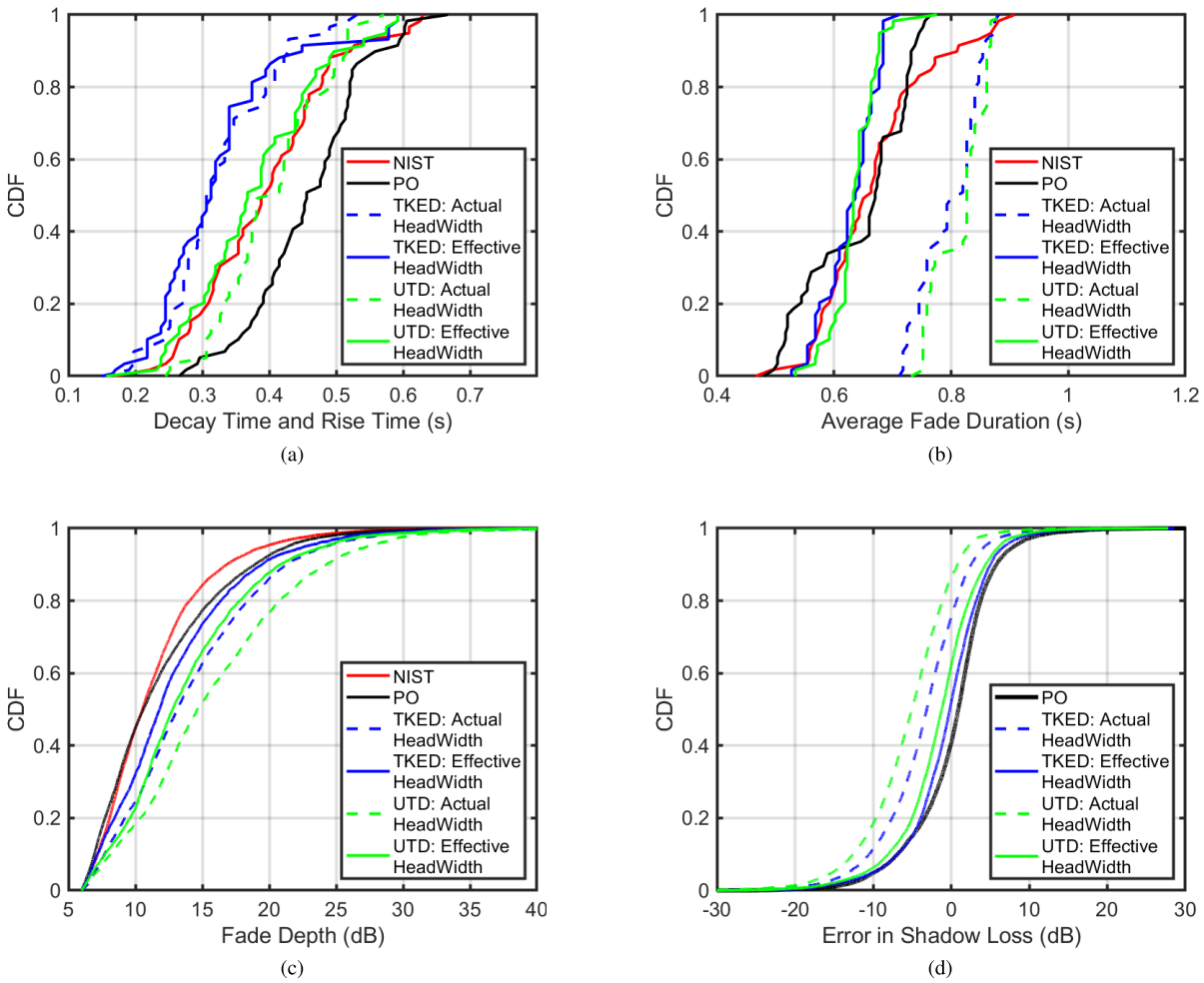

FIGURE 10. CDFs for the three prediction methods and for the measurements of the (a) decay time and rise time, (b) average fade duration and (c) fade depth. (d) CDFs of the error between the three prediction methods and the measurements.[3]

the time in between, demarcating the deep shadow region. Following [27], we used a threshold of -6 dB in this work. Finally, the FD is defined as shadow loss in the deep shadow region of each profile. The four parameters and the deep shadow region are depicted in Fig. 2. Cumulative distribution functions (CDFs) compiled across the 60 scenarios are shown in Fig. 10(a-d). For the TKED and UTD methods, two cases were considered: the actual head depths in Table 1 and the effective head depths — the actual head depths scaled by a tuning factor of 0.8 — a value found empirically to provide the best overall fit between the predictions and measurements. Note that the measured head depths were of the largest extent from the back of the head to the tip of the nose; hence, the effective head depth is an appropriate representation.

Fig. 10(a) shows the CDF of the aggregate decay time and rise time; thanks to symmetry of the setup and of the body, no statistically significant difference between the two was observed and so they were aggregated for simplicity. The UTD agrees best with the measurement, while the PO overestimates and the TKED underestimates the measured value. Also, the use of the effective head depth does not significantly change the UTD and the TKED results obtained with the actual head depth.

Fig. 10(b) displays the CDFs for the AFD. Both the UTD and the TKED methods overestimate the measured AFD when using the actual head depth; however, when using the effective head depth they both slightly underestimate it. The PO method also underestimates the measured AFD, yet it still performs better than both the UTD and the TKED methods when using the effective head depth. Also, note that all three methods fail to capture the tail of the measured AFD distribution, with the TKED methods being the worst while the PO and the UTD methods perform similarly.

Fig. 10(c) compares the CDFs of the fade depth predicted by the three methods and the measurements. In particular,

[3]The first two sub-figures are less smooth because we have only 60 statistical points for decay/rise times and the AFD. However, the FD data points correspond to shadow loss points which lie below the defined threshold level as shown in Fig. 2. We have more than 10000 data points for sub-figures (c) and (d) and hence, their CDFs look smoother.

TABLE 2. Estimated timing parameters.

	Measure-ments	TKED		UTD		PO
		Actual H_d	Effective H_d	Actual H_d	Effective H_d	
Mean Decay and Rise (s)	0.3945	0.3240	0.3241	0.4041	0.3798	0.4577
Mean AFD (s)	0.6668	0.7975	0.6276	0.8150	0.6351	0.6418
Mean Total Fade Time (s)	1.0614	1.1215	0.9517	1.2190	1.0149	1.0995

TABLE 3. Mean error and aggregate RMSE in shadow loss.

	TKED		UTD		PO
	Actual H_d	Effective H_d	Actual H_d	Effective H_d	
Mean Error (dB)	-3.6	-0.6	-5.5	-1.6	0.21
Aggregate RMSE (dB)	6.68	5.39	7.86	5.58	5.46

we focus on the 80th and 90th percentiles to gauge how each method performs in the deep shadow region, where prediction is critical. The PO method clearly outperforms the other two here, overestimating shadow loss by 1.62 dB at the 80th percentile and by 2.1 dB at the 90th percentile. The TKED method with the actual head depth overestimates the measurements by 4.3 dB at the 80th percentile and by 4.6 dB at the 90th percentile, whereas the UTD method with the actual head depth overestimates by 6.7 dB at the 80th percentile and by 7.5 dB at the 90th percentile. Shadow loss predicted by both the TKED and the UTD methods improves when used with the effective head depth: the TKED overestimates by 2.3 dB at the 80th percentile and by 2.7 dB at the 90th percentile, while the UTD overestimates by 3.8 dB at the 80th percentile and by 4 dB at the 90th percentile.

Similar conclusions about the three methods can also be drawn from the estimated timing parameters in Table 2. In summary, the TKED method with the effective head depth fails to capture the tails of the AFD, decay time and rise time distribution and hence, underestimates the total fading time (decay time + AFD + rise time). The total measured fading time is better predicted by both the PO and the UTD with the effective head depth, with the PO slightly overestimating it and the UTD slightly underestimating it.

Finally, Fig. 10(d) displays the CDFs of the errors compiled across all samples in the deep shadow region and across all 60 scenarios, between the three prediction methods and the measurements; Table 3 displays the mean and the aggregate RMSE, computed from these errors. When using the actual head depths, the TKED and UTD methods return considerably greater errors than the PO method, but the errors are comparable when using the effective head depth. Table 4 summarizes the trade-offs between the three prediction methods.

TABLE 4. Trade-offs between the three prediction methods.

Method	Runtime per Simulation	Advantages	Limitations
TKED	Least (≈0.1 sec)	• Fast • Accurately predicts shadow loss when the vertical strip is normal to incident rays	• Cannot model 3D human shapes • Difficult to scale to 3D propagation scenarios • Less accurate in shadowing timing parameter prediction when compared to the other two methods
UTD	Medium (Modified hexagon with 1 diffraction/ray: ≈2 sec)	• Moderately fast • Capable of analysing 3D human shapes • Scalable to 3D propagation scenarios • Predicts shadow timing parameters with best accuracy	• Less accurate in shadow loss prediction when compared to the other two methods
PO	Highest (Human Phantom: ≈8 sec)	• Capable of analyzing full 3D human phantom • Provides best prediction of human shadow loss	• Not as scalable as UTD for 3D propagation scenarios due to high computational needs

VI. CONCLUSION

In this article, we compared shadow loss from human blockage predicted through the TKED, UTD, and PO methods in Remcom's *WaveFarer* ray-tracing suite against 60 GHz measurements provided by NIST. The PO method yielded an aggregate RMSE of 5.46 dB and the closest match to the fade depth, with a difference of 1.6 dB to 2 dB in the deep shadow region. The TKED method was the second best for predicting shadow loss, with an aggregate RMSE of 5.4 dB, but it overestimated fade depth by 2.3 dB to 2.7 dB. The UTD method fell just short of the TKED method in estimating shadow loss, with a slightly higher aggregate RMSE of 5.58 dB, and it overestimated the fade depth by 3.8 dB to 4 dB; however, it outperformed the TKED method in total fade duration, which was also best predicted by the PO method.

Although popular application of the TKED method on the vertical strip shape is fast, it lacks 3D representation of the human body; hence, it is accurate only when the strip is normal to incident rays. For 3D representation, the strip must be reoriented perpendicular to each of the incident rays, increasing complexity significantly. While the PO method can be applied to the 3D phantom shape when accuracy is paramount, it suffers from high computational complexity. On the other hand, the UTD method applied to the hexagon shape provides 3D representation, is computationally scalable to complex scenes, and provides accuracy that is comparable to the PO method. Therefore, for modeling human blockage in complex 3D ray-tracing simulations, the UTD-hexagon approach is recommended.

ACKNOWLEDGMENT

The authors would like to thank anonymous reviewers at Remcom for their valuable suggestions.

REFERENCES

[1] T. S. Rappaport, S. Sun, R. Mayzus, H. Zhao, Y. Azar, K. Wang, G. N. Wong, J. K. Schulz, M. Samimi, and F. Gutierrez, "Millimeter wave mobile communications for 5G cellular: It will work!" *IEEE Access*, vol. 1, pp. 335–349, 2013.

[2] T. Rappaport, Y. Xing, G. R. MacCartney, A. F. Molisch, E. Mellios, and J. Zhang, "Overview of millimeter wave communications for fifth-generation (5G) wireless networks-with a focus on propagation models," *IEEE Trans. Antennas Propag.*, vol. 65, no. 12, pp. 6213–6230, Dec. 2017.

[3] Y. Niu, Y. Li, D. Jin, L. Su, and A. V. Vasilakos, "A survey of millimeter wave communications (mmWave) for 5G: Opportunities and challenges," *Wireless Netw.*, vol. 21, no. 8, pp. 2657–2676, Nov. 2015.

[4] J. Kibilda, A. B. MacKenzie, M. J. Abdel-Rahman, S. K. Yoo, L. G. Giordano, S. L. Cotton, N. Marchetti, W. Saad, W. G. Scanlon, A. Garcia-Rodriguez, D. Lopez-Perez, H. Claussen, and L. A. DaSilva, "Indoor millimeter-wave systems: Design and performance evaluation," *Proc. IEEE*, vol. 108, no. 6, pp. 923–944, Jun. 2020.

[5] L. Zhang, Y. Hua, S. L. Cotton, S. K. Yoo, C. R. C. M. Da Silva, and W. G. Scanlon, "An RSS-based classification of user equipment usage in indoor millimeter wave wireless networks using machine learning," *IEEE Access*, vol. 8, pp. 14928–14943, 2020.

[6] 3GPP. *Study on Channel Model for Frequencies from 0.5 to 100 GHz*. Accessed: Feb. 15, 2022. [Online]. Available: https://portal.3gpp.org/desktopmodules/Specifications/SpecificationDetails.aspx?specificationId=3173

[7] S. Y. Jun, C. Lai, D. Caudill, J. Wang, J. Senic, N. Varshney, and C. Gentile, "Quasi-deterministic channel propagation model for 60 GHz urban Wi-Fi access from light poles," *IEEE Antennas Wireless Propag. Lett.*, vol. 21, no. 8, pp. 1517–1521, Aug. 2022.

[8] M. Ghaddar, L. Talbi, and T. A. Denidni, "Human body modelling for prediction of effect of people on indoor propagation channel," *Electron. Lett.*, vol. 40, no. 25, p. 1592, Dec. 2004.

[9] M. Ghaddar, L. Talbi, T. A. Denidni, and A. Sebak, "A conducting cylinder for modeling human body presence in indoor propagation channel," *IEEE Trans. Antennas Propag.*, vol. 55, no. 11, pp. 3099–3103, Nov. 2007.

[10] J. Kunisch and J. Pamp, "Ultra-wideband double vertical knife-edge model for obstruction of a ray by a person," in *Proc. IEEE Int. Conf. Ultra-Wideband*, Sep. 2008, pp. 17–20.

[11] M. Jacob, S. Priebe, T. Kürner, M. Peter, M. Wisotzki, R. Felbecker, and W. Keusgen, "Extension and validation of the IEEE 802.11 ad 60 GHz human blockage model," in *Proc. 7th Eur. Conf. Antennas Propag. (EuCAP)*, 2013, pp. 2806–2810.

[12] J. S. Lu, D. Steinbach, P. Cabrol, and P. Pietraski, "Modeling human blockers in millimeter wave radio links," *ZTE Commun.*, vol. 10, no. 12, pp. 23–28, Dec. 2012.

[13] G. R. MacCartney, S. Deng, S. Sun, and T. S. Rappaport, "Millimeter-wave human blockage at 73 GHz with a simple double knife-edge diffraction model and extension for directional antennas," in *Proc. IEEE 84th Veh. Technol. Conf. (VTC-Fall)*, Sep. 2016, pp. 1–6.

[14] M. Jacob, S. Priebe, A. Maltsev, A. Lomayev, V. Erceg, and T. Kürner, "A ray tracing based stochastic human blockage model for the IEEE 802.11 ad 60 GHz channel model," in *Proc. 5th Eur. Conf. Antennas Propag. (EUCAP)*, 2011, pp. 3084–3088.

[15] N. Tran, T. Imai, and Y. Okumura, "Study on characteristics of human body shadowing in high frequency bands: Radio wave propagation technology for future radio access and mobile optical networks," in *Proc. IEEE 80th Veh. Technol. Conf. (VTC-Fall)*, Sep. 2014, pp. 1–5.

[16] X. Chen, L. Tian, P. Tang, and J. Zhang, "Modelling of human body shadowing based on 28 GHz indoor measurement results," in *Proc. IEEE 84th Veh. Technol. Conf. (VTC-Fall)*, Sep. 2016, pp. 1–5.

[17] M. Yokota, T. Ikegamai, Y. Ohta, and T. Fujii. *Numerical Examination of EM Wave Shadowing by Human Bodies Between Transmitter and Receiver*. Accessed: Feb. 15, 2022. [Online]. Available: http://ap-s.ei.tuat.ac.jp/isapx/2010/pdf/185.pdf

[18] M. Jacob, C. Mbianke, and T. Kurner, "A dynamic 60 GHz radio channel model for system level simulations with MAC protocols for IEEE 802.11 ad," in *Proc. IEEE Int. Symp. Consum. Electron. (ISCE)*, Jun. 2010, pp. 1–5.

[19] C. Gustafson and F. Tufvesson, "Characterization 60 GHz shadowing by human bodies simple phantoms," in *Proc. 6th Eur. Conf. Antennas Propag. (EUCAP)*, 2012, pp. 473–477.

[20] M. Peter, M. Wisotzki, M. Raceala-Motoc, W. Keusgen, R. Felbecker, M. Jacob, S. Priebe, and T. Kurner, "Analyzing human body shadowing at 60 GHz: Systematic wideband MIMO measurements and modeling approaches," in *Proc. 6th Eur. Conf. Antennas Propag. (EUCAP)*, Mar. 2012, pp. 468–472.

[21] A. G. Aguilar, P. H. Pathak, and M. Sierra-Pérez, "A canonical UTD solution for electromagnetic scattering by an electrically large impedance circular cylinder illuminated by an obliquely incident plane wave," *IEEE Trans. Antennas Propag.*, vol. 61, no. 1, pp. 5144–5154, Oct. 2013.

[22] M. Benzaghta, R. B. Coruk, B. Yalcinkaya, and A. Kara, "An experimental study on the influence of human movement in indoor radio channel at 28 GHz," in *Proc. IEEE Int. Black Sea Conf. Commun. Netw. (BlackSeaCom)*, May 2021, pp. 1–3.

[23] G. R. MacCartney, T. S. Rappaport, and S. Rangan, "Rapid fading due to human blockage in pedestrian crowds at 5G millimeter-wave frequencies," in *Proc. IEEE Global Commun. Conf.*, Dec. 2017, pp. 1–7.

[24] X. Zhao, Q. Wang, S. Li, S. Geng, M. Wang, S. Sun, and Z. Wen, "Attenuation by human bodies at 26- and 39.5-GHz millimeter wavebands," *IEEE Antennas Wireless Propag. Lett.*, vol. 16, pp. 1229–1232, 2017.

[25] Y. Dalveren, G. Karatas, M. Derawi, and A. Kara, "A simple propagation model to characterize the effects of multiple human bodies blocking indoor short-range links at 28 GHz," *Electronics*, vol. 10, no. 3, p. 305, Jan. 2021.

[26] *WaveFarer Reference Manual*, Remcom, State College, PA, USA, Nov. 2020.

[27] A. Bhardwaj, D. Caudill, C. Gentile, J. Chuang, J. Senic, and D. G. Michelson, "Geometrical-empirical channel propagation model for human presence at 60 GHz," *IEEE Access*, vol. 9, pp. 38467–38478, 2021.

[28] U. T. Virk and K. Haneda, "Modeling human blockage at 5G millimeter-wave frequencies," *IEEE Trans. Antennas Propag.*, vol. 68, no. 3, pp. 2256–2266, Mar. 2020.

[29] R. Sun, P. B. Papazian, J. Senic, Y. Lo, J.-K. Choi, K. A. Remley, and C. Gentile, "Design and calibration of a double-directional 60 GHz channel sounder for multipath component tracking," in *Proc. 11th Eur. Conf. Antennas Propag. (EUCAP)*, Mar. 2017, pp. 1–5.

[30] G. James, *Geometrical Theory of Diffraction for Electromagnetic Waves*, 3rd ed. Edison, NJ, USA: IET, 1986.

[31] B. R. Levy, "Diffraction by an elliptic cylinder," *J. Math. Mech.*, vol. 9, no. 2, pp. 147–165, Nov. 1960.

[32] C. A. Balanis, *Advanced Engineering Electromagnetics*, 2nd ed. Hoboken, NJ, USA: Wiley, 2012.

[33] C. Gentile, F. Valoit, and N. Moayeri, "A raytracing model for wireless propagation in tunnels with varying cross section," in *Proc. IEEE Global Commun. Conf. (GLOBECOM)*, Dec. 2012, pp. 5027–5032.

[34] T. Wu, T. S. Rappaport, and C. M. Collins, "The human body and millimeter-wave wireless communication systems: Interactions and implications," in *Proc. IEEE Int. Conf. Commun. (ICC)*, Jun. 2015, pp. 2423–2429.

[35] A. R. Miller, R. M. Brown, and E. Vegh, "New derivation for the rough-surface reflection coefficient and for the distribution of sea-wave elevations," *IEE Proc. H-Microw., Opt. Antennas*, vol. 131, no. 2, p. 114, 1984.

SWAGATO MUKHERJEE received the B.Tech. degree in electronics and communications from the West Bengal University of Technology, Kolkata, India, in 2012, the M.S. degree in electrical engineering from IIT Madras, Chennai, India, in 2015, and the Ph.D. degree in electrical engineering from The Ohio State University, Columbus, OH, USA, in 2020. He is currently an RF Propagation Engineer with Remcom, State College, PA, USA. His research interests include computational electromagnetics, signal processing, remote sensing, wireless communications, and indoor and outdoor propagation.

GREGORY SKIDMORE received the B.S. degree in electrical engineering from the University of Virginia, in 1993, and the M.S. degree in electrical engineering from Johns Hopkins University, in 1997. He is currently the Director of Propagation Software & Government Services at Remcom. His current interests include channel modeling, automotive radar drive scenario modeling, and radar analysis.

TARUN CHAWLA (Member, IEEE) received the B.S. degree in electrical engineering from Pennsylvania State University, in 2008. He joined Remcom, in 2009, and he is currently the Director of Business Development. His research interest includes millimeter-wave channel modeling.

ANMOL BHARDWAJ received the B.A.Sc. and M.A.Sc. degrees in electrical and computer engineering from The University of British Columbia, Vancouver, BC, Canada. He worked as a Guest Researcher with the Communications Technology Laboratory, National Institute of Standards and Technology, from October 2017 to December 2018, where he has been a Guest Researcher with the Communications Technology Laboratory, since November 2019. His research interests include millimeter-wave channel measurements and modeling.

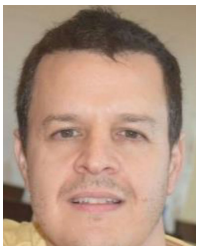

CAMILLO GENTILE (Member, IEEE) received the Ph.D. degree in electrical engineering from Pennsylvania State University, in 2001. He joined the National Institute of Standards and Technology, Gaithersburg, MD, USA, in 2001, where he is currently leading the Radio Access and Propagation Metrology Group and the NextG Channel Measurement and Modeling Project with the Communications Technology Laboratory. He has authored over 100 peer-reviewed journals and conference papers, a book on geolocation techniques, and a book on millimeter-wave and sub-terahertz channel propagation modeling. His current interests include channel modeling and physical-layer modeling for 5G and 6G wireless systems.

JELENA SENIC received the B.S. and M.S. degrees in electrical engineering from the University of Belgrade, Belgrade, Serbia, in 2009 and 2010, respectively. Since January 2015, she has been a Researcher with the National Institute of Standards and Technology, Boulder, CO, USA. Her current research interests include radio propagation channel measurements and modeling at millimeter-wave frequencies. The team in which she works was a recipient of the Best Measurement Paper Award at EuCAP 2017.